DE GRUYTER Open Geosciences 2025; 17: 20220759

Research Article

Fanrong Wei, Xinzhi Yan, Yubin Bai*, Yanjun Bai, and Kai Zhou

Effect of pore throats on the reservoir quality of tight sandstone: A case study of the Yanchang Formation in the Zhidan area, Ordos Basin

https://doi.org/10.1515/geo-2022-0759
received June 03, 2024; accepted December 23, 2024

Abstract: Due to the tight sandstone widespread development of nanoscale pore-throat systems, the microscopic pore-throat characteristics of tight reservoirs are the focus of research. Taking the main tight oil production province of the Ordos Basin in China as a case study, nuclear magnetic resonance (NMR), pressure-controlled mercury injection (PMI), scanning electron microscopy, and micro-computed tomography (μCT) are used to analyze the characteristics of four types of tight sandstones with different pore throats. Furthermore, the effects of pore throats on movable fluid, connectivity, and reservoir physical properties are analyzed. The results show that the pore throats of the four types of tight sandstones are obviously different, but they are all dominated by nanoscale pore-throat systems. From types I to IV, the pore types of the tight sandstone change from residual intergranular pores to the coexistence of feldspar dissolved pores and residual intergranular pores and then to the coexistence of residual intergranular pores and intergranular micropores. The T_2 NMR spectrum changes from a double peak to a single peak, the pore-throat connectivity revealed by μCT decreases from 83.8% for type I to 13.1% for type IV, the pore-throat volume ratio revealed by PMI decreases from 2.09 to 0.43, and the NMR movable fluid saturation decreases from 38.91 to 12.39%. Tight sandstone with larger pores and a uniform distribution has high movable fluid saturation and good pore-throat connectivity. Although the tight sandstone with dissolved pores and intergranular pores may have a medium porosity, the pore–throat connectivity deteriorates compared with high porosity sandstone. Large pore throats, which account for less than 15% of all pore throats, contribute more than 90% of the permeability, while pore throats less than 0.8 μm in diameter are major contributors to the reservoir space, and both the porosity and permeability decrease as the pore-throat diameter decreases.

Keywords: tight sandstone, pore structure characterization, pore-throat connectivity, Yanchang formation, Ordos Basin

1 Introduction

Tight sandstone is an important reservoir type for the formation and accumulation of unconventional hydrocarbons. Unlike conventional sandstone reservoirs with good physical properties, tight sandstone reservoirs are distributed mainly near source rocks [1–3] and exhibit complex pore-throat systems along with obvious heterogeneity [4–6], nanoscale pore-throat [2,6–10], and non-Darcy flow [11–13]. Tight sandstone has attracted increasing attention due to its large petroleum geological reserves and significant contribution to unconventional hydrocarbon production [14]. However, in tight sandstone, pore-throat systems with different scales ranging from a few nanometers to hundreds of microns have developed, and the pore-throat connectivity is poor [15–17]; therefore, comprehensively and accurately characterizing the pore structure of tight sandstone is highly challenging [10,18,19]. The pore throat of tight sandstone not only controls the reservoir quality, hydrocarbon-bearing properties, and producibility [20,21] but also controls the processes of hydrocarbon charging, migration and accumulation, and the degree of enrichment [12] and has a very important influence on the accurate evaluation of hydrocarbon geological reserves and development strategies [22]. The microscopic pore structure in tight sandstone reservoirs is a major problem [23–25].

In recent years, multiple advanced testing methods have been widely applied to study the microscopic pore throats of tight reservoirs, including field-emission scanning electron microscopy (FE-SEM), micro/nano-computed

---

* **Corresponding author: Yubin Bai,** School of Earth Sciences and Engineering, Xi'an Shiyou University, Xi'an, Shaanxi, 710065, China, e-mail: baiyubin@xsyu.edu.cn
Fanrong Wei, Xinzhi Yan, Yanjun Bai: Yanchang Oilfield Co., Ltd., Yan'an, Shaanxi, 716000, China
Kai Zhou: School of Earth Science and Resources, Chang'an University, Xi'an, Shaanxi, 710054, China

tomography (CT), rate-controlled mercury injection (RMI), pressure-controlled mercury injection (PMI), and nuclear magnetic resonance (NMR) [15,18,22,26,27], which have enabled significant progress in the understanding of microscopic pore throats in tight reservoirs.

However, different test techniques have significant differences in the sample size, shape, test principle, and procedure of experimentation [15,28–30], resulting in the test results of the same sample often not completely matching. Only pores larger than a few microns can be observed and counted in cast thin sections, and the large number of nanosized pores cannot be counted. The imaging accuracy of rock samples polished by argon ions can reach 5 nm [23], but the area is only approximately 1.5 mm × 0.5 mm [31], and the pores can only be observed and statistically measured in two dimensions; the pore-throat connectivity cannot be effectively obtained also. The maximum resolution of micro-CT (μCT) is approximately 1 μm, but the corresponding sample size is only 1–5 mm [32], and nanoscale pore throats cannot be characterized. The effective resolution of nano-CT is 50 nm, but the sample size is only 65 μm [19,29]. Because of the strong heterogeneity of tight sandstone reservoirs and poor representativeness of small samples, the pore distribution scale that can be characterized is limited.

Fluid injection technology cannot directly visualize pores, but it can fully reflect the pore structure. The maximum mercury injection pressure in PMI reaches 200 MPa, which reflects the overall distribution characteristics for pore throat size between 4 nm and 1 mm [26]; its disadvantage is that pores cannot be separated from throats. Although the pores and throats can be separated by RMI, the maximum mercury injection pressure is only 6.2 MPa, which can only indicate pore throats with sizes greater than 0.12 μm [4]; this does not meet the accuracy required for pore structure research in tight reservoirs. The T_2 spectrum curve can be acquired by NMR technology, which can indicate the distribution of pores through transformation. The prerequisite is to obtain an accurate relaxation rate and key parameters of the pore shape factor [28,33]. Therefore, each technique has some deficiencies in comprehensively displaying the microscopic pore throats of tight reservoirs, and a single technique has difficulty fully reflecting the complex pore throats of tight sandstone. Multimethod, multiscale, and multidimensional comprehensive characterization of the microscopic pore throats of tight sandstone is the key to effectively addressing the shortcomings of each approach [4,26,34–39].

Many researchers have characterized the microscopic feature of the total pore size of tight sandstone by integrating NMR, RMI, PMI, scanning electron microscopy (SEM), and μCT [8,19,26,40–44]. A full-scale, accurate description of tight reservoir microscopic pore throats is necessary; however, the main purpose of research on hydrocarbon reservoirs is exploration and production. How the micropore structure influences and controls the reservoir's physical properties and how the fluid moves in pore throats of different scales are two important aspects related to the reservoir storage and transfer capacity.

Recently, a few scholars have focused on the effect of pore throats on reservoir physical properties. The controlling effect of the pore-throat size on the tight sandstone quality and oil content is that the permeability is predominantly contributed by larger pore throats with a proportion of less than 30% [25,38]; however, smaller pore throats are very important to the reservoir capacity, and hydrocarbons are mainly distributed in pore throats with radii of 0.1–1 μm. The permeability in tight reservoirs is effectively controlled by the maximum pore-throat radius, and the volume of throats greatly contributes to the total porosity [45]. The small throats are the main influencing factor of pore connectivity and low permeability, and throats with a radius greater than 0.2 μm account for less than 40% of porosity but contribute more than 95% of permeability [46]. The pore throats smaller than 0.1 μm in tight sandstone have little effect on the permeability but provide an important pore space for petroleum accumulation [47].

Using a case study of the Yanchang Formation in the Zhidan area of the Ordos Basin, this article studies the pore types, pore-throat sizes, and distribution characteristics of tight sandstone in the Yanchang Formation by using thin section casting, SEM, NMR, PMI, and μCT. On this basis, the control of the movable fluid and connectivity by the pore-throat size is confirmed, and the contributions of pore throats of different sizes to the reservoir porosity and permeability are clarified.

2 Samples and experiments

2.1 Sample collection and experimental process

The samples were acquired from the upper Triassic Yanchang Formation in the Zhidan area, central southern Shanbei Slope, Ordos Basin. Fifteen samples of fine sandstone and siltstone with different oil-bearing characteristics were collected from three wells evenly distributed throughout the study area (Figure 1). The classification standard mainly considers the relationship between reservoir physical properties, oil test production, and oil-bearing occurrence: the tight reservoir of

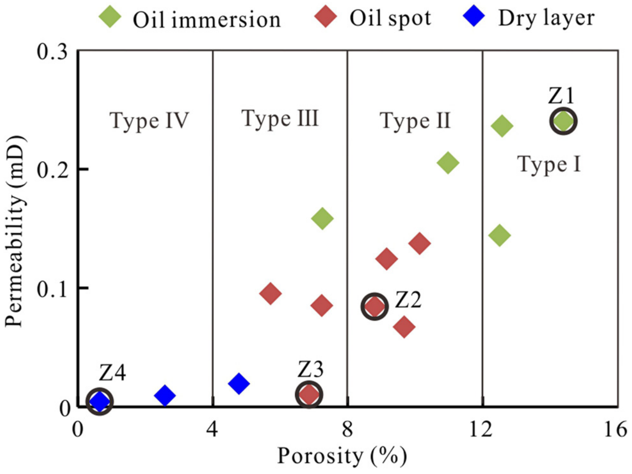

Figure 1: Relationships between the porosity, permeability, and oil appearance of the tight sandstone in the Zhidan area, Ordos Basin.

Yanchang Formation is an ineffective reservoir when the porosity is less than 4%, and the sweet spot in the tight reservoir when the porosity is more than 12%. Reservoirs with porosity between 8 and 12% are the main producing reservoirs of tight oil, which are dominated by industrial oil flow Wells, while those with porosity between 4 and 8% are the secondary producing reservoirs, which are mostly dominated by low–producing Wells. Fifteen regular cylindrical experimental samples were collected parallel to the formation direction in the uniform lithology section, with a diameter of approximately 2.5 cm and an average length of approximately 4 cm. The remaining oil and salt in the samples were washed with an alcohol and benzene mixture, and the samples were then air–dried. The samples were dried at 100°C for 24 h and cooled to room temperature for 12 h before the helium porosity and nitrogen permeability were measured. The test method conformed to the industry standard SY/T 5336-2006 [48]. After the samples were dried again, samples with a thickness of 0.5 cm were cut from the edge of the core column to make thin slices for casting and prepare the SEM samples. The cast thin slices were prepared in accordance with the oil and gas industry standard SY/T 5913-2004 [49], and the sample preparation and identification conformed to the oil and gas industry standard SY/T 5162-2014 [50].

2.2 Experimental methods

2.2.1 Thin section casting

A total of 15 tight sandstone samples from the Yanchang Formation were used to prepare cast thin sections. Ethanol was mixed with benzene at a ratio of 1:3 to remove residual oil from the core. Blue epoxy resin was injected into the core at room temperature under a pressure of 6 MPa, and thin sections with a thickness of 0.03 mm were prepared. The mineral composition and content, clay minerals, and pore types were observed and analyzed under single and orthogonal polarized light using a Leica DM750 polarizing microscope.

2.2.2 Scanning electron microscopy (SEM)

The core samples were mechanically cut and sprayed with 10 nm of platinum on the fresh surface. A Quanta 200 F FE-SEM produced by the FEI Company of Holland with a resolution of 3.5 nm, an amplification of 25-200000, and an acceleration voltage of 30 kV was used. The pore morphology and types, size, and cements of the cores were observed under a vacuum of 6×10^{-4} Pa.

2.2.3 X-ray diffraction of clay minerals

The samples were washed with oil and dried in an electric drying oven at 60°C. After cooling to room temperature, the sample was pulverized to a particle size less than 1 mm, after which the sample was ground to a particle size less than 40 μm. The clay minerals with particle sizes less than 10 and 2 μm were extracted by the water suspension separation method. The total percentage of clay minerals in the rock was determined based on samples with particle sizes less than 10 μm, and the relative value of each clay mineral was determined based on samples with particle sizes less than 2 μm.

2.2.4 NMR

The NMR instrument used was a MARAN-2 measuring instrument, and the experimental temperature was set at 25°C. The echo interval of the NMR instrument was 0.6 ms, the waiting time was 6 s, the echo number was 2048, and the scanning time was 128. After the sample was completely saturated with simulated formation water with a salinity of 30,000 mg/L, NMR measurements were performed, and the porosity of the sample was calculated. The samples saturated with simulated formation water were placed in a PC-1 centrifuge and centrifuged at high speed for 1 h under centrifugal forces of 0.14, 0.29, 1.43, and 2.88 MPa [51]. After centrifugation, NMR measurements were performed on samples in the current water saturation state to obtain T_2 spectra under a saturated water state and different centrifugal force states. The NMR experimental procedures were based on the Chinese standard “Specification for normalization measurement of core NMR parameter in the laboratory” (SY/T 6490-2014) [52].

2.2.5 X-ray computed tomography (μCT)

According to the SEM and cast thin section results, small cylinders with a diameter and a height of 2 mm were drilled from the well-developed pore area in the core for μCT, and the rest of the samples were tested by PMI. The μCT experimental instrument used was an Xradia 520 Versa microscope with an accelerating voltage of 90 kV and a maximum resolution of 0.7 μm. μCT scanning was carried out on a 2 mm diameter sample with a resolution of 1.2 μm. A total of 1,000 2D images were obtained for each sample, and the exposure time of each image was 30 s. Avizo Fire 9.0 software was used to numerically reconstruct 2D images to establish a 3D pore-throat model. The porosity of the sample was acquired based on the percentage of pore-throat volume to sample volume. The details of μCT scans have also been discussed by other scholars [15].

2.2.6 PMI

The PMI experimental instrument used was a PoreMaster PM33-13; the sample length was 2.5 cm, the maximum mercury injection pressure was 116 MPa, and the reflected pore-throat radius was 6 nm. After the NMR and μCT experiments, the samples were dried and then subjected to the PMI experiment. Liquid mercury was injected from low pressure to high pressure to reach the maximum mercury injection pressure, and the samples were discharged, with a drop in the pressure, to obtain mercury injection and mercury withdrawal curves. For the detailed implementation, see China’s oil and gas industry standard SY/T 5346-2005 [53].

3 Results

3.1 Reservoir characteristics of typical samples

Based on the observed lithology and oil appearance characteristics and the reservoir’s physical properties, the tight sandstones of the Yanchang Formation in the Zhidan area of the Ordos Basin can be divided into four types (Figure 1). One representative sample of each type was selected for NMR and μCT analyses (Table 1). The four typical samples

Table 1: Lithology, oil appearance, and physical and mineral compositions of the four types of tight sandstones in the Zhidan area, Ordos Basin

Sample	Type	Lithology	Oiliness	Depth (m)	φ_{He} (%)	Permeability (mD)	Total clay content (%)	Illite (%)	Kaolinite (%)	Chlorite (%)	Illite/smectite (%)
Z1	I	Fine sandstone	Oil immersion	1802.38	14.04	0.24	1.8	22	11	49	18
Z2	II	Fine sandstone	Oil spot	2160.36	8.81	0.084	2.6	32	17	35	16
Z3	III	Fine sandstone	Oil spot	1985.65	6.86	0.01	2.5	41	13	29	17
Z4	IV	Siltstone	Dry layer	2023.39	0.66	0.004	3.2	51	2	10	37

were taken from sandstone cores in delta-lake sedimentary systems. The samples of type I and type III represent the microfacies of the underwater distributary channel in the delta front sub-facies. They are all fine-grained arkosic sandstone with good particle sorting, and the particle size is mainly distributed in the range of 50–200 μm. Type II is a sandy clastic flow in gravity flow deposition, with poor particle sorting and different particle sizes. Type IV is the microfacies of underwater natural levees with medium sorting degree, and the particle size is mainly distributed in 5–50 μm.

The gas permeability and porosity of the four representative samples range from 0.004 to 0.24 mD and 0.66 to 14.04%, respectively. The average amount of cement in tight sandstone is 10.35%, in which the average amount of calcite is 6.44%, and the average amount of clay minerals is 2.54%. The clay minerals are mainly chlorite and illite, the secondary minerals are illite–smectite-mixed beds, and the kaolinite content is the lowest (Table 1).

3.2 Pore types

The cast thin section and SEM results reveal that there are three principal pore types in the samples: residual intergranular pores, intragranular feldspar dissolved pores, and intercrystalline micropores. The morphology of the residual intergranular pores is irregular, and the pore diameter is usually larger than 20 μm (Figure 2a). Chlorite films often develop on the surface of particles with a thickness of 5–10 μm (Figure 2b). The development of chlorite films effectively inhibits the growth of quartz and plays a constructive role in maintaining primary pores [54,55]. The pore diameters of the dissolved feldspar particles are generally 20–50 μm and reach 200 μm (Figure 2c). The intercrystalline micropores of the clay minerals are mostly chlorite and illite, and the pore diameter is less than 1 μm (Figure 2d–f). Type I is composed of residual intergranular pores, type II is primarily composed of intergranular pores, feldspar dissolved pores, and clay mineral micropores, and types III and IV are primarily composed of intercrystalline micropores and a small amount of intergranular pores.

3.3 NMR

3.3.1 T_2 spectrum characteristics of saturated water

The transverse NMR delay times (T_2) of the four types of samples are evenly distributed between 0.1 and 1,000 ms, and all the samples exhibit bimodal distribution

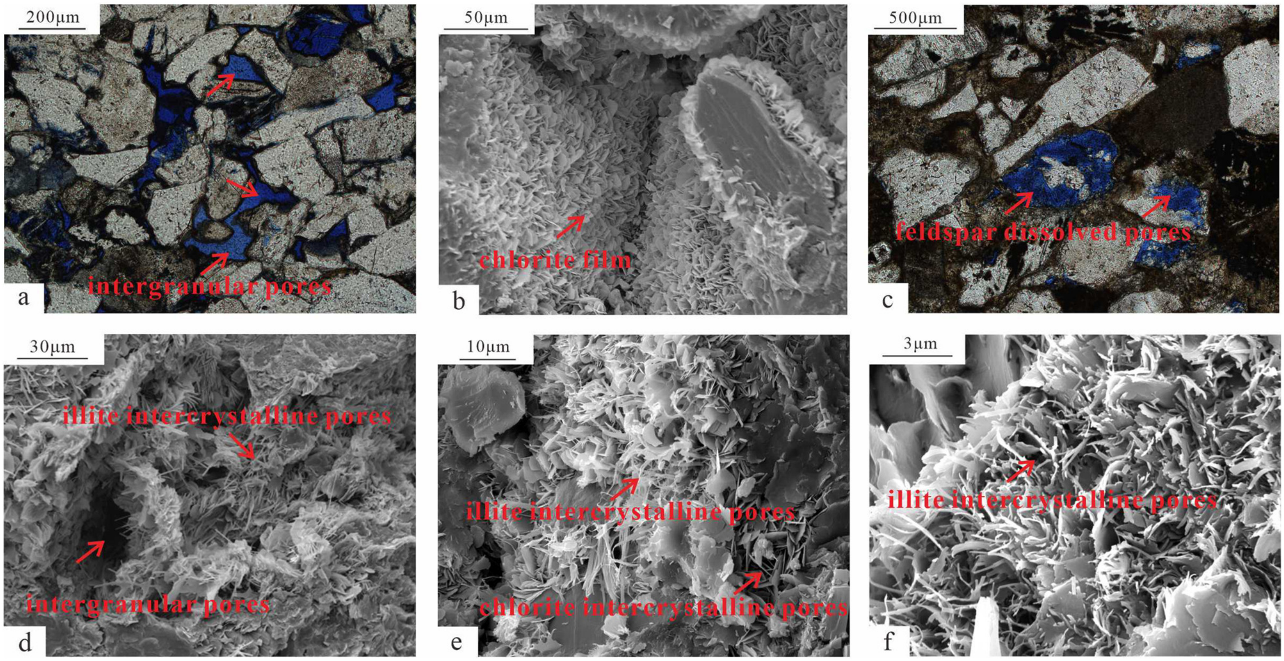

Figure 2: Pore types of the tight sandstone samples in the Zhidan area, Ordos Basin. (a) Residual intergranular pores, type I. (b) Chlorite film, residual intergranular pores, type I, SEM image. (c) Dissolved pores in feldspar grains, type II. (d) Illite intercrystalline pores, residual intergranular pores, type II, SEM image. (e) Illite and chlorite intercrystalline pores, type III, SEM image. (f) Illite intercrystalline pores, type IV, SEM image.

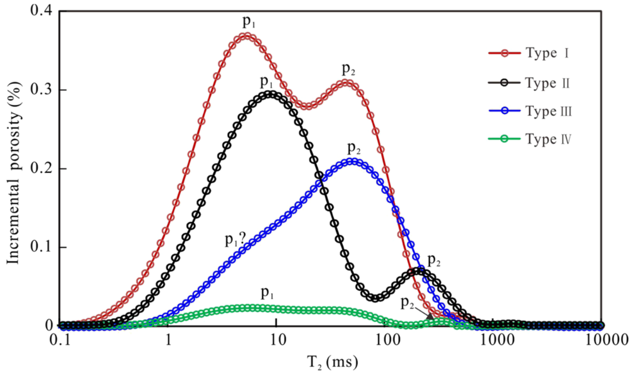

Figure 3: NMR T_2 characteristics of the four types of tight sandstone samples from the Zhidan area, Ordos Basin.

characteristics (P_1 and P_2 peaks), in which the bimodal characteristics of types I and II are obvious, while the bimodal distribution is not obvious for types III and IV (Figure 3). The distribution ranges of the P_1 peak are basically the same (3–20 ms), while the distribution ranges of the P_2 peak are larger (30–400 ms). The P_2 peak ranges are the same (30–70 ms) for types I and III, and the P_2 peak ranges are similar (150–400 ms) for types II and IV. In the bimodal distributions of types I, II and IV, the height of the left peak is greater than that of the right peak, indicating that relatively small pores are dominant. In terms of the difference between the heights of the left peak and the right peak, the left peak of type I is slightly higher than the right peak, and the connection between them indicates that small pores are dominant and that the connectivity between large and small pores is good. The height of the left peak of type II is much greater than that of the right peak, and the continuity of the left peak and the right peak is poor, reflecting the absolute dominance of small pores and poor connectivity between large and small pores. In type III, the P_1 peak is not obvious, while the P_2 peak is prominent, indicating macropores. Type IV has a low porosity, and the P_2 peak is not obvious.

3.3.2 Characteristics of the T_2 spectra for different centrifugal forces

Figure 4 shows the variation in the porosity components reflected by the T_2 NMR spectra of the four typical samples with the centrifugal force. As the centrifugal force

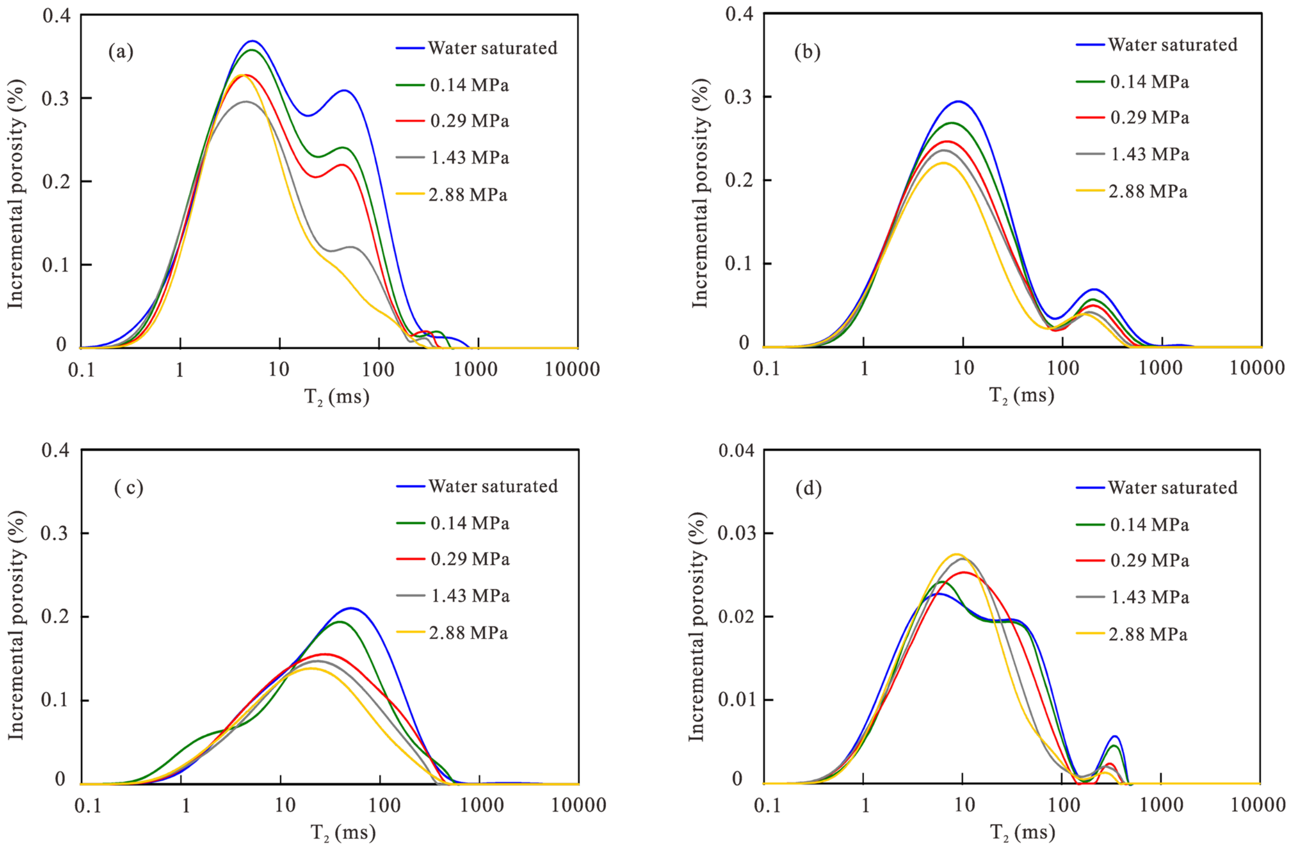

Figure 4: Under different centrifugal force conditions, the variation in the porosity components reflected by the T_2 NMR spectra of the four types of tight sandstones in the Zhidan area of the Ordos Basin. (a) Type I. (b) Type II. (c) Type III and (d) Type IV.

increases from 0.14 to 2.88 MPa, the porosity of the separated movable fluid gradually increases. Except for type IV, the types are dominated by large pores. In type I, with increasing separation pressure, the amplitudes of the P_1 and P_2 peaks decrease, but the P_2 peak decreases more, and the P_2 peak disappears when the separation pressure reaches 2.88 MPa (Figure 4a), indicating that the connectivity of large pores is better than that of small pores. However, the morphology of the P_1 peak changes little after centrifugation, indicating poor connectivity of small pores. At the same time, the concave point connecting the P_1 and P_2 peaks disappears after centrifugation, reflecting good connectivity between small pores and large pores. In type II, the amplitudes of the P_1 and P_2 peaks decrease with increasing centrifugal pressure, but the P_1 peak decreases more, indicating good connectivity of small pores. The T_2 spectral characteristics for the 2.88 MPa centrifugal force and saturated water are similar, but the main P_1 and P_2 peaks shift in the direction of small pores after centrifugation (Figure 4b). In type III, with increasing centrifugal force, the P_2 peak amplitude gradually decreases, and the main peak shifts in the direction of small pores, while the P_1 peak does not significantly change (Figure 4c), indicating that the connectivity of large pores is good, but the connectivity of small pores with large pores is poor. In type IV, the amplitude of the P_1 peak increases while that of the P_2 peak decreases (Figure 4d). Since the concave point connecting the P_1 and P_2 peaks does not change, the connectivity between small pores and large pores is poor.

3.4 μCT

3.4.1 Pore diameter distribution characteristics

The μCT analysis results of the four typical samples reveal that in terms of the total number of pores (Table 2), type II has the most pores, up to 84,626, followed by type III, with 48,022 pores. The numbers of pores for types I and IV are almost the same, which are 35,707 and 34,256, respectively. The pore diameters are divided into three intervals (Table 2): 1–5 μm, 5–10 μm, and 10–200 μm. The smaller the pore diameter, the greater the number of pores. The pore number histogram of pores in different size ranges indicates that the larger the pore diameter, the smaller the number of pores, and the pore number gradually decreases (Figure 5).

The number of pores is closely related to the type of pore. Type II has the largest number of pores because its pore types are predominantly intercrystalline pores of clay minerals and dissolved pores in feldspar particles (Figure 5b); thus, the pore size is small, and the number of pores is large. Type III also has more pores because the pore types are mainly intercrystalline pores of clay minerals and residual intergranular pores after intense diagenesis (Figure 5c). The diagenesis of type I is relatively weak. Due to the protection of the chlorite film, residual intergranular pores develop, and the pore size of a single pore is large, so the number of pores is small (Figure 5a). Type IV has the most complex diagenesis, and the pores are extremely undeveloped. The intercrystalline pores of clay minerals are the main pore type, so the number of pores is small (Figure 5d). The distribution characteristics of the number and types of pores determined based on μCT are basically consistent with the abovementioned results of cast thin section identification.

3.4.2 Pore volume distribution characteristics

The pore volume is consistent with the pore size distribution, and the larger the pore diameter, the larger the pore volume. Pores with a large volume of 10–200 μm dominate in all four typical samples (Table 2). The pore volumes of types I and II are mainly controlled by pores with sizes of 20–200 μm, that of type III is predominantly controlled by pores with sizes ranging from 20–60 μm, and that of type IV is predominantly controlled by pores with sizes ranging from 20 to 40 μm (Figure 5). From type I to type IV, the scale of the pore development gradually decreases, and the pore size interval controlling the main pore volume distribution gradually decreases, as does the equivalent pore diameter interval.

Table 2: Quantitative parameters obtained by μCT of tight sandstone in the Zhidan area, Ordos Basin

Type	Equivalent diameter (μm)	Pore count	Pore area (μm²)	Pore volume (μm³)	$\varphi_{\text{micro-CT}}$ (%)	
I	1–5	31,081	711,677	377,595	7.94	0.15
	5–10	3,959	808,685	650,945		0.27
	10–200	667	9,061,782	18,402,504		7.52
II	1–5	77,314	1,493,742	1,090,716	5.34	0.44
	5–10	6,528	1,378,149	1,454,583		0.60
	10–200	784	5,776,751	10,504,429		4.30
III	1–5	41,886	4,133,182	523,955	6.13	0.21
	5–10	5,390	537,419	865,072		0.36
	10–200	746	7,574,137	13,558,816		5.56
IV	1–5	27,868	2,993,077	864,533	3.56	0.35
	5–10	5,395	743,869	1,709,321		0.70
	10–200	993	424,395	6,130,401		2.51

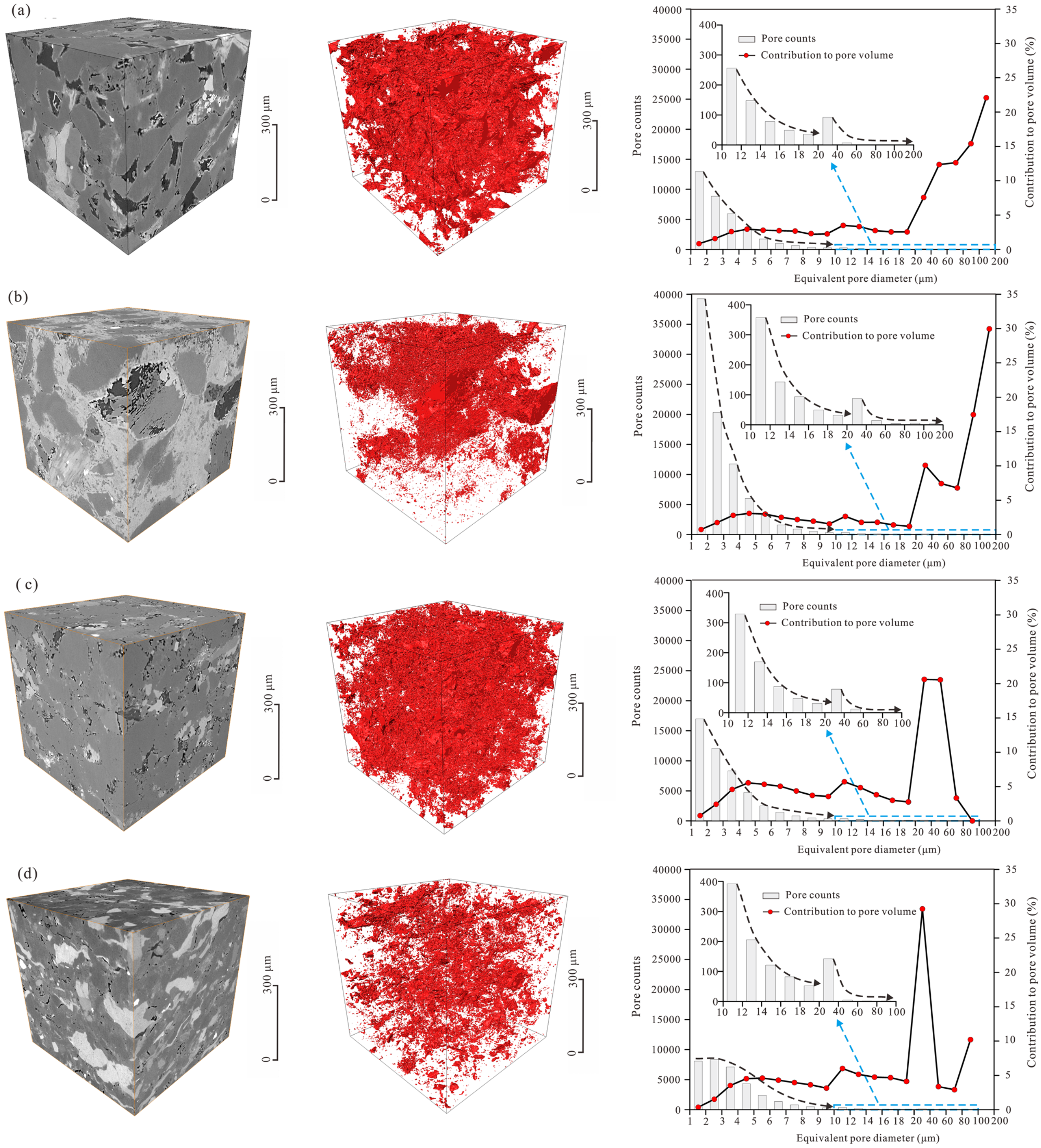

Figure 5: μCT images of the 3D material phase model and pore model of the four types of tight sandstones in the Zhidan area, Ordos Basin. The pore quantity and equivalent pore size and their contributions to the pore volume were quantitatively extracted using Avizo Fire 9.0 software. (a) Type I. (b) Type II. (c) Type III and (d) Type IV.

3.5 PMI

3.5.1 Mercury injection curve characteristics

Based on the morphological characteristics of the mercury injection curves of the four typical samples, from type I to type IV, with the decrease in the porosity and permeability, the threshold pressure increases from 1.05 to 5.68 MPa, and the maximum mercury saturation decreases from 86.21 to 15.53%, indicating successive deterioration of the reservoir pore structure (Table 3 and Figure 6a). The comparison shows that the plateau segment of the mercury injection curves of types I, II, and III is obvious, reflecting good pore structure and connectivity, but the main throat diameter of type III is less than 0.1 μm, indicating that the pores are mainly clay mineral-dominated micropores. Type IV has the worst pore structure, with no plateau section and a maximum mercury saturation of only 15.53%.

3.5.2 Pore-throat distribution characteristics

According to the capillary action principle and the Washburn equation [56], the relation between the pore-throat radius and mercury injection pressure is

$$r_c = 2\sigma \cos\theta / P_c, \tag{1}$$

where r_c is the pore-throat radius, μm; σ is the surface tension between mercury and air, N/m; θ is the wetting contact angle between mercury and air, °; and P_c is the mercury inlet capillary pressure, MPa.

The σ and θ between mercury and air are 0.48 N/m and 140°, respectively. The following formula can be obtained according to equation (1):

$$r_c = 0.735/P_c. \tag{2}$$

According to equation (2), the radius of the pore throats can be obtained, and then the diameter of the pore throats can be calculated. In the four types of samples, the pore-throat diameters are between 0.01 and 2 μm, and the large distribution range is mainly related to the coexistence of different pore types. From type I to type IV, the maximum mercury saturation gradually decreases, the drainage pressure continuously increases, and the pore-throat diameter changes from relatively large to small (Figure 6), reflecting that the pore structure of the reservoir changes from good to poor. The results show that the distribution characteristics of the pore-throat diameters of types I and II are generally consistent (Figure 6b and c), and the pore-throat diameter distribution range is wide (0.1–1 μm). However, type I is absolutely dominated by a single pore-throat diameter and presents a single-peak distribution, while the pore-throat diameters of type II present a double-peak distribution; the main peak is consistent with that of type I, with a peak value of 0.3 μm, and the secondary peak corresponds to a pore-throat diameter of 0.05 μm (Figure 7). The main pore-throat diameters of types III and IV are less than 0.1 μm (Figures 6d and e, and 7). The pore-throat diameters for type III exhibit a single-peak distribution, and the major pore-throat diameter is 0.03 μm (Figure 7). For type IV, the maximum main peak is still not displayed at the experimental maximum charging pressure of 116 MPa, suggesting that the pore-throat diameter corresponding to

Table 3: Pore-throat characteristic parameters of tight sandstone in the Zhidan area, Ordos Basin from PMI

Type	Porosity (%)	Permeability (mD)	Threshold pressure (MPa)	Medium saturation pressure (MPa)	Relative sorting coefficient	Maximum pore-throat radius (μm)	Medium pore-throat radius (μm)	Average pore-throat radius (μm)	Maximum mercury intrusion saturation (%)	Residual mercury saturation (%)	Mercury extrusion efficiency (%)	Pore/throat volume ratio
I	14.04	0.24	1.05	6.74	0.21	0.344	0.109	0.169	86.21	58.30	32.37	2.09
II	8.81	0.084	1.23	23.58	0.37	0.239	0.031	0.135	71.20	44.50	37.50	1.67
III	6.86	0.01	3.24	91.08	0.42	0.048	0.012	0.039	66.85	43.30	35.23	1.84
IV	0.66	0.004	5.68	/	2.15	0.010	/	0.036	15.53	4.70	69.74	0.43
Average	7.59	0.085	2.80	40.47	0.79	0.160	0.051	0.095	59.95	37.70	43.71	1.51

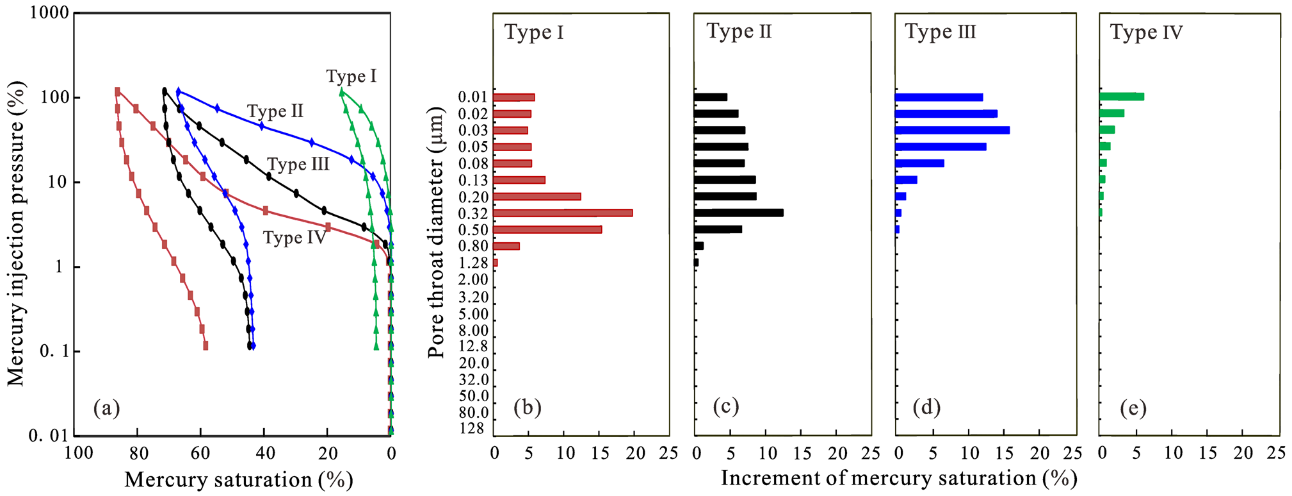

Figure 6: Mercury injection curves and pore-throat diameter characteristics of the four types of typical tight sandstones in the Zhidan area, Ordos Basin. (a) Type I. (b) Type II. (c) Type III and (d) Type IV.

the maximum real-time mercury saturation may be less than 0.01 µm (Figure 7).

4 Discussion

4.1 Pore-throat diameter control of movable fluid

The content and distribution characteristics of movable fluid are the primary factors influencing the quality and production of tight sandstones. The water in the pores of tight sandstone reservoirs mainly includes movable water and irreducible water. Irreducible water is clay-bound water and capillary water (BVI) residing in micropores, while movable (free) water (FFI) fills in macropores [57]. By analyzing the NMR T_2 spectrum of saturated water, essential parameters such as the effective porosity, total porosity, NMR permeability, and saturation of movable and bound fluids can be obtained. The $T_{2\text{cut-off}}$ value that distinguishes the bound and movable fluids must be determined first [16,28,58,59].

NMR centrifugation is designed to expel movable water from macropores and is theoretically based on equation (1). In equation (1), for simplification purposes, σ and θ between water and air are taken as 0.073 N/m and 0°, respectively. As a result, equation (1) becomes

$$r_c = 0.146/P_c. \tag{3}$$

In the NMR experiment of this study, the centrifugal forces of 0.14, 0.29, 1.43 and 2.88 MPa correspond to pore diameters of 2.0, 1.0, 0.2 and 0.1 µm, respectively, according to equation (3). The T_2 spectrum after centrifugation at a centrifugal force of 2.88 MPa corresponds to two types of bound water: one type is bound water controlled by micro-capillary for throats smaller than 0.1 µm, and the other type is a bound water film on the surface of macropores. The method for determining the $T_{2\text{-cutoff}}$ value is shown in Figure 8. The $T_{2\text{cut-off}}$ value determined in this study corresponds to a 2.88 MPa centrifugal force, which is basically consistent with the value of 2.76 MPa determined by Li et al. [60] for the Chang 7 tight sandstone of the Yanchang Formation in the Ordos Basin.

The $T_{2\text{cut-off}}$ values of the four types of tight sandstones range from 16.76 to 57.06 ms, and the associated movable fluid saturation ranges from 12.39 to 38.91% (Table 4). In

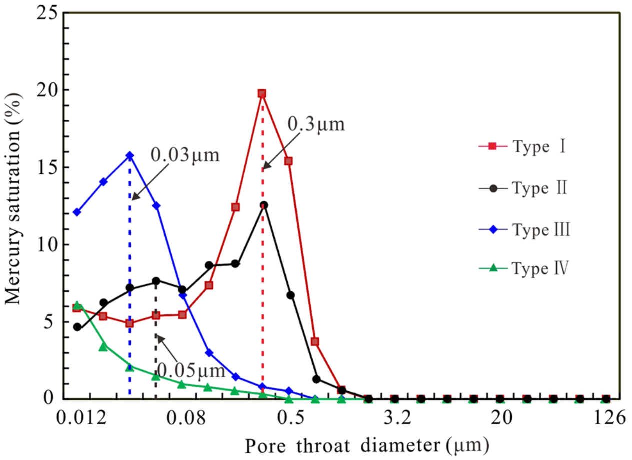

Figure 7: Pore-throat diameter distribution of tight sandstone in the Zhidan area, Ordos Basin.

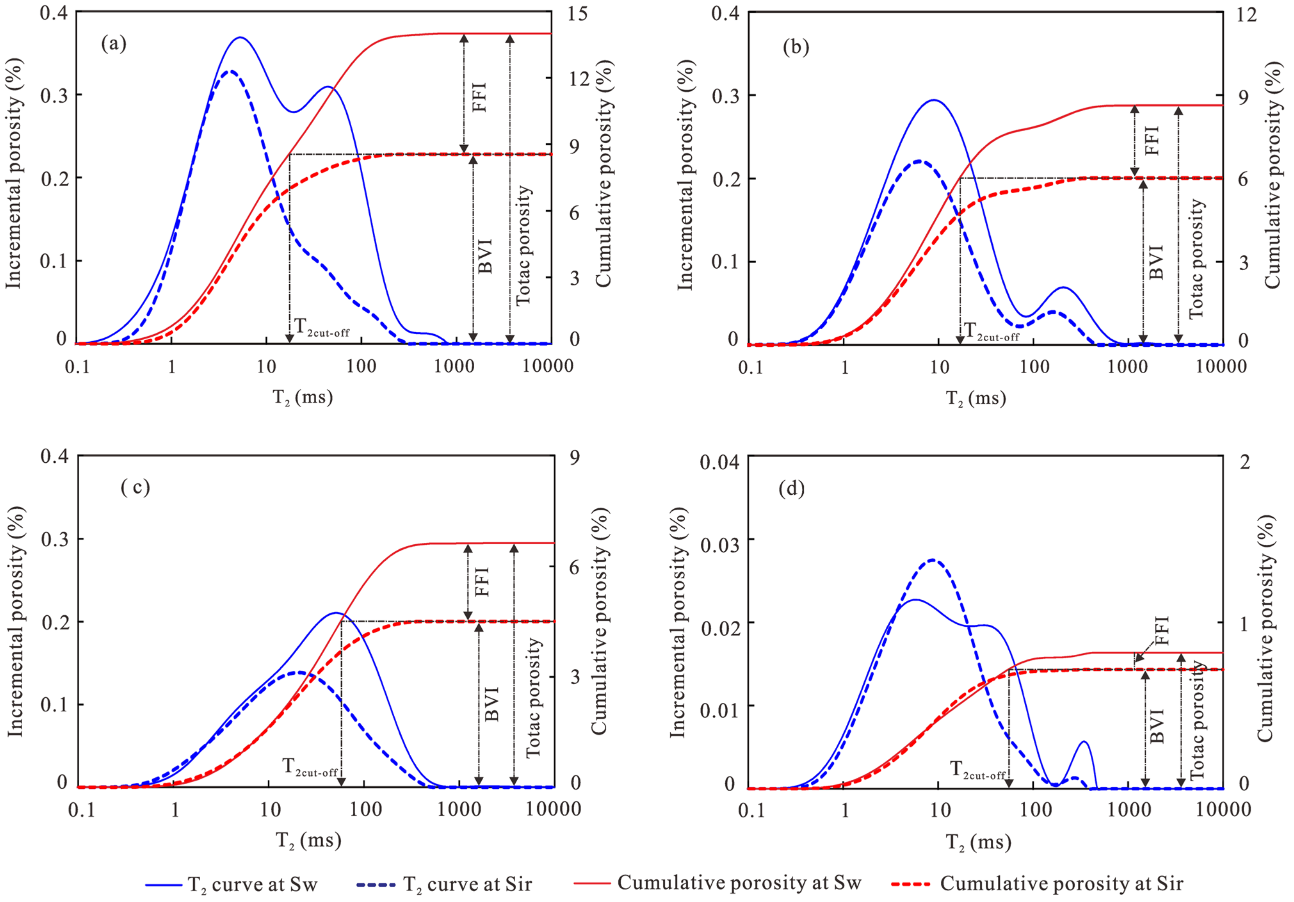

Figure 8: Incremental porosity and total porosity distribution determined from NMR T_2 spectra under 100% water and bound water conditions of typical samples in the Ordos Basin and their determined $T_{2\text{cut-off}}$ values. (a) Type I. (b) Type II. (c) Type III and (d) Type IV.

general, with increasing permeability and porosity, $T_{2\text{cut-off}}$ decreases, and the movable fluid saturation increases. After the removal of the irreducible water contribution from the NMR data, the FFI and BVI were computed to range from 0.10 to 5.44% and 0.72 to 8.55%, respectively (Table 4). The FFI and BVI values show a large range, and the BVI is much greater than the FFI, implying that the reservoir space is dominated by nanometer pores with irreducible fluids. The FFI/BVI ratio ranges from 0.44 to 0.64, except for type IV (Table 4), which indicates moderate seepage capacity and reservoir connectivity [57].

In this article, the evaluation criteria proposed by Zhu et al. [61] were used for classification of pores in oil and gas reservoirs. Based on the pore diameter (P_d), the pore system can be divided into millipores (P_d > 1 mm), micropores (1 μm < P_d < 1,000 μm), submicropores (0.1 μm < P_d < 1 μm), and nanopores (P_d < 100 nm). In the four types of pore-throat systems, the proportion of movable fluid in the

Table 4: Distribution characteristics of NMR movable fluid in the Yanchang Formation in the Zhidan area, Ordos Basin

Type	Permeability	φ_{He}	φ_{NMR}	$T_{2\text{cut-off}}$ (ms)	FFI	BVI	FFI/BVI	Movable fluid saturation (%)	Movable fluid saturation controlled by pore diameter (%)			
	(mD)	(%)	(%)		(%)	(%)			*d* > 2 μm	1 μm > *d* > 2 μm	0.2 μm > *d* > 1 μm	0.1 μm > *d* > 0.2 μm
I	0.24	14.04	13.99	17.27	5.44	8.55	0.64	38.91	11.75	9.04	12.08	6.05
II	0.084	8.81	8.64	16.76	2.63	6.01	0.44	30.38	10.59	6.86	5.14	7.79
III	0.01	6.86	6.63	57.06	2.13	4.50	0.47	32.09	9.36	7.80	10.20	4.73
IV	0.004	0.66	0.82	54.55	0.10	0.72	0.14	12.39	4.91	2.19	3.26	2.03

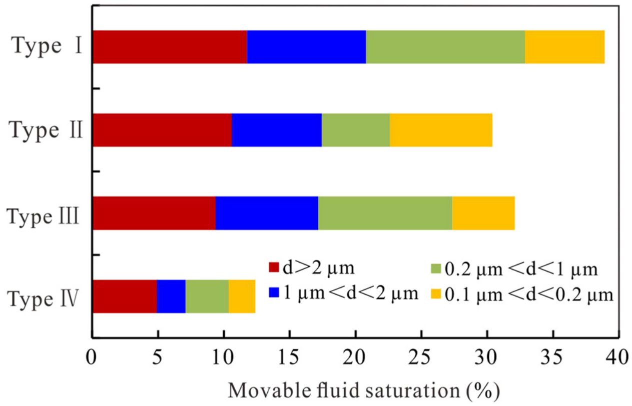

Figure 9: Distribution histogram of movable fluid dominated by the pore diameters in the Zhidan area, Ordos Basin.

micropores is 53.43–57.44% (Figure 9 and Table 4), regardless of the level of porosity. Based on the four pore sizes controlled by the centrifugal force, micropores larger than 2 μm and submicropores between 0.2 and 1 μm are dominant in types I, III, and IV, whereas type II is dominated by pores with diameters greater than 2 μm and pores ranging in size from 0.1 to 0.2 μm (Figure 9). This finding is consistent with the research of Wu et al. [51] on the Chang 7 member in the Yanchang Formation, in which movable fluid was concluded to mostly occur in pore throats with diameters ranging from 0.2–2 μm.

4.2 Pore-throat diameter control of connectivity

Microscopic-nanoscale pores coexist in the four types of tight sandstones in the Yanchang Formation in the Zhidan area, and nanoscale pore throats are dominant (79.21–92.9%). The proportion of micropores (with an average of 15.6%) is slightly greater than that of submicropores (with an average of 12.82%). The μCT data reflect the total porosity of the sample and the porosities of the four types of tight sandstones range from 3.56 to 7.94% (Table 5). The μCT porosity is lower than the helium porosity for types I, II, and III because nitrogen porosity reflects the total pore volume at the micron and nanoscale. For type IV, the μCT porosity is significantly greater than the helium porosity, which reflects the heterogeneity of the sample, and the test location of μCT is relatively porous. The percentage of micron-sized connected pores in the total porosity successively decreases from types I to IV, with values of 83.8, 56.0, 71.2, and 13.1%. The proportion of connected pores in type III is greater than that in type II, showing that the type III pore throats are evenly distributed (Figure 4c) and have good pore-throat connectivity. From types I to IV, the micropore connectivity gradually deteriorates.

The nanoscale pore-throat connectivity can be demonstrated by PMI, where the mercury saturation of the injection in PMI corresponds to the bulk volume of the pores and throats, while the ejection saturation reflects only the proportion occupied by throats, so the residual mercury saturation reveals the proportion of the rock pore volume [62]. The calculated pore-throat volume ratio is shown in Table 1. The pore-throat volume ratio of type I is 2.09, which corresponds to the best connectivity, while the pore-throat volume ratio of type IV is only 0.43, which corresponds to the worst connectivity. Types III and II are in the middle. In terms of the reservoir space of tight sandstone, the pore volume proportions of types I, II, and III are greater than the throat volume proportions, while the main contribution in type IV is from the throat volume.

4.3 Pore-throat diameter control of the reservoir quality

The PMI analysis of the four types of tight sandstones shows that the pore-throat diameters that contribute most to the permeability correspond to the few micropores or submicropores in the samples. The cumulative permeability contribution (CPC) rapidly increases at the peak pore-throat diameter position, and when the CPC reaches 90%, the cumulative mercury intake generally does not exceed 15% (Figure 10a–d); that is, the large pore throats in the samples, which account for less than 15% of all pore throats, contribute more than 90% of the permeability. In types I and II, pore throats with diameters less

Table 5: Porosity measured by different methods and calculation parameters for tight sandstone in the Zhidan area, Ordos Basin

Type	Permeability (mD)	φ_{He} (%)	$\varphi_{\text{micro-CT}}$ (%)	$\varphi_{\text{micro-CT}}/\varphi_{\text{He}}$ ratio (%)	Connected pore volume based on micro-CT (%)
I	0.24	14.04	7.94	56.55	83.8
II	0.084	8.81	5.34	60.61	56.0
III	0.01	6.86	6.13	89.36	71.2
IV	0.004	0.66	3.56	539.39	13.1

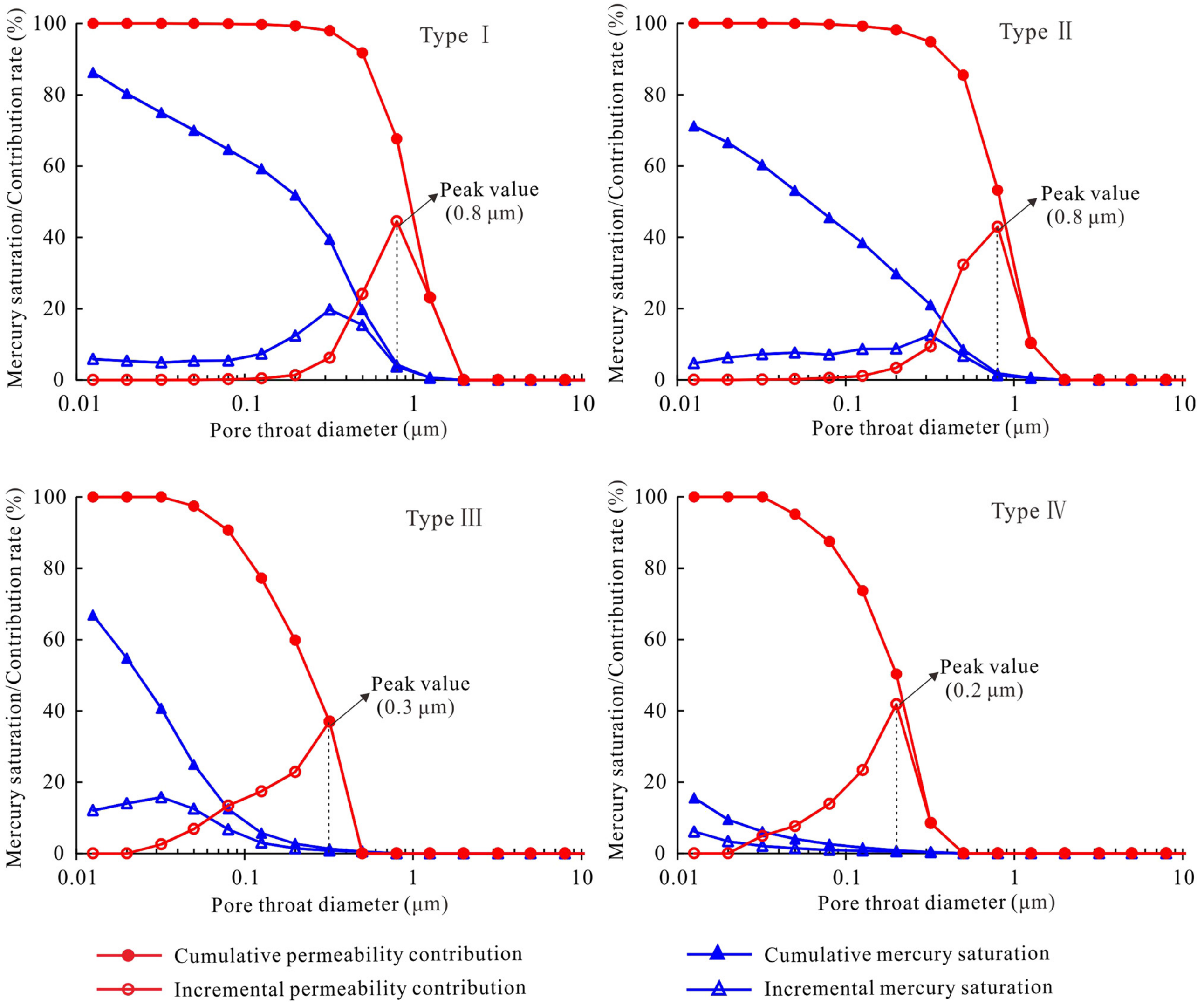

Figure 10: Comparison of the contribution of pore-throat diameters to the storage and transfer capacity of tight sandstone in the Zhidan area, Ordos Basin.

than 0.3 μm contribute little to the permeability, while the pore-throat diameters of types III and IV have wide distributions, and pore throats with diameters less than 0.04 μm contribute little to the permeability. For the type I sample with a 0.24 mD permeability in Figure 10a, when the CPC reaches 90%, the cumulative mercury volume is only approximately 13.8%. However, for the type III sample with a permeability of 0.01 mD in Figure 10c, when the CPC reaches 90%, the cumulative mercury volume is only approximately 6.5%. The permeability of the tight sandstone reservoir is predominantly influenced by the large pore throats in the samples, which occupy a very small volume.

Submicropores and nanopores account for most of the volume but contribute little to the permeability, and the lower the permeability is, the greater the relative ratio of small pore throats (Figure 10a–d). The pore-throat volume of type I is principally controlled by the submicron scale, the pore-throat volume of type II is controlled by both the submicron and nanometer scales, and the pore-throat volumes of types III and IV are principally dominated by the nanometer scale.

5 Conclusions

The pore-throat characteristics of different types of tight sandstones in the Ordos Basin were studied by multiple test techniques. The main conclusions are as follows:

(1) Based on the reservoir lithology, physical properties and oil appearance characteristics, the tight sandstone in the Zhidan area can be divided into four types. Type

I contains residual intergranular pores, type II contains residual intergranular pores and feldspar dissolved pores, and types III and IV are dominated by intragranular micropores.

(2) The T_2 spectra of tight sandstones of types I and II are bimodal, while those of tight sandstones of types III and IV are mainly unimodal. The average pore diameter from μCT is mainly larger than 10 μm, and the main pore diameters of types I and II are larger than 20 μm and up to 200 μm. The average pore diameter of type III is mostly within 20–70 μm, and that of type IV is mostly within 20–50 μm. The main peak values of the pore-throat diameters corresponding to types I and II are 0.3 μm that corresponding to type III is 0.03 μm, and that corresponding to type IV is less than 0.01 μm.

(3) The saturations of movable fluid for the four types revealed by NMR are 12.39–38.91%, and the percentage of movable fluid in the pore throats larger than 1.0 μm is 53.43–57.44%. Movable fluid saturation is dominated by the porosity and permeability of the reservoir.

(4) Except for type IV, the percentage of micron-scale connected pore throats in the total pore-throat volume ranges from 56.0–83.8%. Type I and type III pore throats have weak heterogeneity and good connectivity, and type II has the second-best connectivity. The nanoscale pore/throat volume ratio revealed by PMI is 1.67–2.09, except for in type IV, indicating that the pore volume dominates the main reservoir space of tight sandstone, followed by the volume occupied by throats.

(5) The pore throats that mainly contribute to the permeability have diameters of 0.2–0.8 μm, and the peak value of the pore-throat diameter decreases with decreasing permeability. However, the peak diameters of the pore throats that contribute more to the reservoir space are 0.03–0.3 μm, except for in type IV. The permeability is dominated by micron and submicron pore throats, but the submicron and nanometer pore throats are more important for the reservoir space.

Funding information: The authors disclosed receipt of the following financial support for the research, authorship, and/or publication of this article: This work was supported by the Key Laboratory of the Education Department of Shaanxi Province (No. 18JS090) and the Natural Science Foundation of Shaanxi Province (No. 2017JM4014).

Author contributions: F.W. contributed and wrote the manuscript. X.Y. contributed to the discussion of the results. Y.B. contributed to guidance and revised the manuscript. Y.B. and K.Z. were responsible for the methods and drawing the map.

Conflict of interest: Authors state no conflict of interest.

References

[1] Zhao J, Bai Y, Cao Q, Er C. Quasi-continuous hydrocarbon accumulation: A new pattern for large tight sand oilfields in the Ordos Basin. Oil Gas Geol. 2012;33(6):811–27.

[2] Zou C, Yang Z, Tao S, Wei L, Wu S, Hou LH, et al. Nano-hydrocarbon and the accumulation in coexisting source and reservoir. Pet Explor Dev. 2012;39(1):15–32.

[3] Bai Y, Zhao J, Zhao Z, Yin Y, Tong J. Accumulation conditions and characteristics of the Chang 7 tight oil reservoir of the the Yanchang Formation in Zhidan area, Ordos Basin. Oil Gas Geol. 2013;34(5):631–9.

[4] Zhu RK, Wu ST, Su L. Problems and future works of porous texture characterization of tight reservoirs in China. Acta Petrolei Sin. 2016;37(11):1323–36.

[5] Zhao J, Li J, Cao Q, Bai Y, Wu W, Ma Y. Quasi-continuous hydrocarbon accumulation: An alternative model for the formation of large tight oil and gas accumulations. J Pet Sci Eng. 2019;174:25–39.

[6] Jiang F, Zhang C, Wang K, Zhao Z, Zhong K. Characteristics of micropores, pore throats, and movable fluids in the tight sandstone oil reservoirs of the Yanchang Formation in the southwestern Ordos Basin, China. AAPG Bull. 2019;103(12):2835–59.

[7] Nelson PH. Pore-throat sizes in sandstones, tight sandstones and shales. AAPG Bull. 2009;93(8):329–40.

[8] Xiao D, Jiang S, Thul D, Huang W, Lu Z, Lu S. Combining rate-controlled porosimetry and NMR to probe full-range pore throat structures and their evolution features in tight sands: A case study in the Songliao Basin, China. Mar Pet Geol. 2017;83:111–23.

[9] Wu H, Zhang CL, Ji YL, Liu RE, Wu H, Zhang YZ. An improved method of characterizing the pore structure in tight oil reservoirs: Integrated NMR and constant-rate-controlled porosimetry data. J Pet Sci Eng. 2018;166:778–96.

[10] Wang G, Jin ZJ, Liu GX, Wang R, Zhao G, Tang X, et al. Pore system of the multiple lithofacies reservoirs in unconventional lacustrine shale oil formation. Int J Coal Geol. 2023;273:104270.

[11] Zeng J, Zhang Y, Zhang S, Qiao J, Feng X, Feng S. Experimental and theoretical characterization of the natural gas migration and accumulation mechanism in low-permeability (tight) sandstone cores. J Nat Gas Sci Eng. 2016;33:1308–15.

[12] Zhang Y, Zeng J, Qiao J, Feng X, Wang F, Ren N. Experimental study on natural gas migration and accumulation mechanism in sweet spots of tight sandstones. J Nat Gas Sci Eng. 2016;36:669–78.

[13] Zhang YC, Zeng JH, Dai ZX, Viswanathan H, Xiao T, Ma Y, et al. Experimental investigation on oil migration and accumulation in tight sandstones. J Pet Sci Eng. 2018;160:267–75.

[14] Zou C, Zhang G, Yang Z, Tao S, Wang Z. Geological concepts, characteristics, resource potential and key techniques of unconventional hydrocarbon: on unconventional petroleum geology. Pet Explor Dev. 2013;40(4):385–99+454.

[15] Desbois G, Urai JL, Hemes S, Schröppel B, Schwarz JO, Mac M, et al. Multi-scale analysis of porosity in diagenetically altered reservoir

sandstone from the Permian Rotliegend (Germany). J Pet Sci Eng. 2016;140:128–48.

[16] Lai J, Wang GW, Wang ZY, Chen J, Pang XJ, Wang SC, et al. A review on pore structure characterization in tight sandstones. Earth-Sci Rev. 2018;177:436–57.

[17] Cao YC, Xi KL, Liu KY, Zhu RK, Yuan GH, Zhang XX, et al. Reservoir properties characterization and its genetic mechanism for tight sandstone oil and gas reservoir in lacustrine basin: The case of the Fourth member of Lower Cretaceous Quantou Formation in the southern Songliao Basin. Acta Petrolei Sin. 2018;39(3):247–65.

[18] Desbois G, Urai JL, Kukla PA, Konstanty J, Baerle C. High-resolution 3D fabric and porosity model in a tight gas sandstone reservoir: a new approach to investigate microstructures from mm-to nm-scale combing argon beam cross sectioning and SEM imaging. J Pet Sci Eng. 2011;78:243–57.

[19] Liu XF, Wang JF, Ge L, Hu FL, Li CL, Yu J, et al. Pore-scale characterization of tight sandstone in Yanchang Formation Ordos Basin China using micro-CT and SEM imaging from nm- to cm-scale. Fuel. 2017;209:254–64.

[20] Sakhaee-Pour A, Bryant SL. Effect of pore structure on the producibility of tight-gas sandstones. AAPG Bull. 2014;98(4):663–94.

[21] Shanley KW, Cluff RM. The evolution of pore-scale fluid-saturation in low-permeability sandstone reservoirs. AAPG Bull. 2015;99(10):1957–90.

[22] Shanley KW, Cluff RM, Robinson JW. Factors controlling prolific gas production from low-permeability sandstone reservoirs: implications for resource assessment, prospect development, and risk analysis. AAPG Bull. 2004;88(8):1083–121.

[23] Loucks RG, Reed RM, Ruppel SC, Hammes U. Spectrum of pore types and networks in mudrocks and a descriptive classification for matrix-related mudrock pores. AAPG Bull. 2012;96:1071–98.

[24] Anovitz LM, Cole DR. Characterization and analysis of porosity and pore structures. Rev Miner Geochem. 2015;80(1):61–164.

[25] Xi KL, Cao YC, Haile BG, Zhu RK, Jahren J, Bjørlykke K, et al.How does the pore-throat size control the reservoir quality and oiliness of tight sandstones? The case of the lower cretaceous Quantou Formation in the Southern Songliao Basin, China. Mar Pet Geol. 2016;76:1–15.

[26] Wu ST, Zhu RK, Li X, Jin X, Yang Z, Mao ZG. Evaluation and application of porous structure characterization technologies in unconventional tight reservoirs. Earth Sci Front. 2018;25(2):191–203.

[27] Li CL, Tan MJ, Wang ZZ. Nuclear magnetic resonance pore radius transformation method and fluid mobility characterization of shale oil reservoirs. Geoenergy Sci Eng. 2023;221:211403.

[28] Yao YB, Liu DM. Petrophysical characterization of coals by low-field nuclear magnetic resonance (NMR). Fuel. 2010;89:1371–80.

[29] Bai B, Zhu RK, Wu ST, Yang WJ, Jeff G, Allen G, et al. Multi-scale method of nano(micro)-CT study on microscopic pore structure of tight sandstone of Yanchang Formation, Ordos Basin. Pet Explor Dev. 2013;40(3):354–8.

[30] Pipintakos G, Hasheminejad N, Lommaert C. Application of atomic force (AFM), environmental scanning electron (ESEM) and confocal laser scanning microscopy (CLSM) in bitumen: A review of the ageing effect. Micron: Int Res Rev J Microsc. 2021;147:103083.

[31] Loucks RG, Reed RM, Ruppel SC, And DM, Jarvie DM. Morphology, genesis, and distribution of nanometer-scale pores in siliceous mudstones of the Mississippian Barnett shale. J Sediment Res. 2009;79(12):848–61.

[32] Zhang P, Lu S, Li J, Zhang P, Xie L, Xue H, et al. Multi-component segmentation of X-ray computed tomography (CT) image using multi-Otsu thresholding algorithm and scanning electron microscopy. Energ Explor Exploit. 2017;35(3):281–94.

[33] Lyu C, Ning Z, Wang Q, Chen M. Application of NMR T_2 to pore size distribution and movable fluid distribution in tight sandstones. Energy Fuels. 2018;32:1395–405.

[34] Clarkson CR, Freeman M, He L, Agamalian M, Melnichenko YB, Mastalerz M, et al. Characterization of tight gas reservoir pore structure using USANS/SANS and gas adsorption analysis. Fuel. 2012;95:371–85.

[35] Clarkson CR, Jensen JL, Pedersen PK, Freeman M. Innovative methods for flow-unit and pore-structure analyses in a tight siltstone and shale gas reservoir. AAPG Bull. 2012;96:355–74.

[36] Gao H, Li HA. Pore structure characterization, permeability evaluation and enhanced gas recovery techniques of tight gas sandstones. J Nat Gas Sci Eng. 2015;28:536–47.

[37] Medina CR, Mastalerz M, Rupp JA. Characterization of porosity and pore-size distribution using multiple analytical tools: Implications for carbonate reservoir characterization in geologic storage of CO_2. AAPG Bull. 2017;24:51–72.

[38] Xi KL, Cao YC, Li K, Liu KY, Zhu RK, Haile BG. Insight into pore-throat size distribution and the controls on oil saturation of tight sandstone reservoirs using nuclear magnetic resonance parameters: A case study of the Lower Cretaceous Quantou Formation in the southern Songliao Basin, China. AAPG Bull. 2020;104(11):2351–77.

[39] Qin Y, Yao SP, Xiao HM, Cao J, Hu WX, Sun LH, et al. Pore structure and connectivity of tight sandstone reservoirs in petroleum basins: a review and application of new methodologies to the Late Triassic Ordos Basin, China. Mar Pet Geol. 2021;129:105084.

[40] Yao YB, Liu DM. Comparison of low-field NMR and mercury intrusion porosimetry in characterizing pore size distributions of coals. Fuel. 2012;95:152–8.

[41] Zhao HW, Ning ZF, Wang Q, Zhang R, Zhao TY, Niu TF, et al. Petrophysical characterization of tight oil reservoirs using pressure-controlled porosimetry combined with rate-controlled porosimetry. Fuel. 2015;154:233–42.

[42] Daigle H, Johnson A. Combining mercury intrusion and nuclear magnetic resonance measurements using percolation theory. Transp Porous Med. 2016;111:669–79.

[43] Wang L, Zhao N, Sima L, Meng F, Guo Y. Pore structure characterization of the tight reservoir: systematic integration of mercury injection and nuclear magnetic resonance. Energy Fuels. 2018;32(7):7471–84.

[44] Zhang LC, Lu SF, Xiao DS, Li B. Pore structure characteristics of tight sandstones in the northern Songliao Basin, China. Mar Pet Geol. 2017;88:170–80.

[45] Zhang YL, Bao ZD, Yang F, Mao SW, Song J, Jiang L. The controls of pore-throat structure on fluid performance in tight clastic rock reservoir: A case from the Upper Triassic of Chang 7 member, Ordos Basin, China. Geofluids. 2018;2:3403026.

[46] Liu GF, Bai YX, Gu DH, Lu Y, Yang DY. Determination of static and dynamic characteristics of microscopic pore-throat structure in a tight oil-bearing sandstone formation. AAPG Bull. 2018;102:1867–92.

[47] Wang JJ, Wu SH, Li Q, Zhang JJ, Guo QH. Characterization of the pore-throat size of tight oil reservoirs and its control on reservoir physical properties: a case study of the Triassic tight sandstone of the sediment gravity flow in the Ordos Basin, China. J Pet Sci Eng. 2020;186:106701.

[48] Qu YT, Dai ZJ, Li GM, Wang S, Jia LH, Zhang Q. Practices for core analysis: SY/T 5336—2006. Beijing: Petroleum Industry Press; 2006.

[49] Li YX, Zhou HY, Yang YF, Bai XM, Liu JC. Rock thin section preparation: SY/T 5913—2004. Beijing: Petroleum Industry Press; 2004.

[50] Wei GZ, Zhu DS, Liu WX, Li XW, Wang B, Xie ZH, et al. Analytical method of rock sample by scanning electron microscope: SY/T 5162—2014. Beijing: Petroleum Industry Press; 2014.

[51] Wu ST, Li SX, Yuan XJ, Yang Z, Li AF, Cui JW, et al. Fluid mobility evaluation of tight sandstones in Chang 7 member of Yanchang Formation, Ordos Basin. J Earth Sci-China. 2021;32(4):850–62.

[52] Luo YY, Wu D, Du HH, Li X, Mao ZQ, Xie RH, et al. Specification for measurement of rock NMR parameter in laboratory: SY/T 6490-2014. Beijing: National Energy Administration, Petroleum Industry Press; 2014.

[53] Zhang ZB, Hong Y, Luo ML. Rock capillary pressure measurement: SY/T 5346-2005. Beijing: Petroleum Industry Press; 2005.

[54] Berger A, Gier S, Krois P. Porosity-preserving chlorite cements in shallow-marine volcaniclastic sandstones: Evidence from Cretaceous sandstones of the Sawan gas field, Pakistan. AAPG Bull. 2009;93(5):595–615.

[55] Sun ZX, Sun ZL, Yao J, Wu ML, Liu JR, Dou Z. Porosity preservation due to authigenic chlorite coatings in deeply buried upper triassic xujiahe formation sandstones, Sichuan Basin, Western China. J Pet Geol. 2014;37(3):251–67.

[56] Washburn EW. The dynamics of capillary flow. Phys Rev. 1921;17(3):273–83.

[57] Timur A. Pulsed nuclear magnetic resonance studies of porosity, movable fluid, and permeability of sandstones. J Pet Technol. 1969;21:775–86.

[58] Dillinger A, Esteban L. Experimental evaluation of reservoir quality in Mesozoic formations of the Perth Basin (Western Australia) by using a laboratory low field nuclear magnetic resonance. Mar Pet Geol. 2014;57:455–69.

[59] Testamanti MN, Rezaee R. Determination of NMR T_2 cut-off for clay bound water in shales: A case study of Carynginia Formation, Perth Basin, Western Australia. J Pet Sci Eng. 2017;149:497–503.

[60] Li HB, Guo HK, Yang ZM, Wang XW. Tight oil occurrence space of Triassic Chang 7 Member in Northern Shaanxi Area, Ordos Basin, NW China. Pet Explor Dev. 2015;42(3):396–400.

[61] Zhu RK, Wu ST, Cui JW. Classification and evaluation of pore size in oil and gas reservoir rock. Geol Sci Technol Inf. 2016;35(3):133–44.

[62] Yu J, Ma J, Lu JG, Cao Y, Feng SB, Li WC. Application of mercury injection and rate-controlled mercury penetration in quantitative characterization of microscopic pore structure of tight reservoirs: a case study of the Chang 7 reservoir in Huachi-Heshui area, the Ordos Basin. Pet Geol Expt. 2015;37(6):790–5.